

# A Multifunctional Nanocomposite Hydrogel for Endoscopic Tracking and Manipulation

Adriana Augurio, Paolo Cortelletti, Riccardo Tognato, Anne Rios, Riccardo Levato, Jos Malda, Mauro Alini, David Eglin, Gabriele Giancane, Adolfo Speghini,\* and Tiziano Serra\*

Herein, the fabrication of multi-responsive and hierarchically organized nano-material using core-shell SrF<sub>2</sub> upconverting nanoparticles, doped with Yb<sup>3+</sup>, Tm<sup>3+</sup>, Nd<sup>3+</sup> incorporated into gelatin methacryloyl matrix, is reported. Upon 800 nm excitation, deep monitoring of 3D-printed constructs is demonstrated. Addition of magnetic self-assembly of iron oxide nanoparticles within the hydrogel provides anisotropic structuration from the nano- to the macro-scale and magnetic responsiveness permitting remote manipulation. The present study provides a new strategy for the fabrication of a novel highly organized multi-responsive material using additive manufacturing, which can have important implications in biomedicine.

Sophisticated nanocomposite hydrogels expressing multifunctionalities and multiscale hierarchical organization can now be fabricated through the combination of a diverse array of nanomaterials within additively manufactured structures.<sup>[1]</sup> External stimulation (e.g., by temperature, optical radiation, pH, electric, or magnetic field) can trigger a broad range of functionalities conferred by the tailored nano-objects conveniently arranged within the hydrogel matrices.<sup>[1–3]</sup>

Furthermore, it is possible to tune a number of structural features into hydrogels on demand.<sup>[1,2]</sup> For example, to recapitulate similar mechanical properties of native extracellular matrix and to stimulate the growth and morphogenesis of specific tissues,


the anisotropy of different biocompatible hydrogels was adjusted.<sup>[2,4]</sup>

Optically-responsive polymers can be used for drug-release application,<sup>[5,6]</sup> real-time in vivo tracking, monitoring of degradation application,<sup>[7,8]</sup> and in situ photocrosslinking.<sup>[9–11]</sup> Fluorescent dyes-based hydrogels, where the organic fluorophores are covalently linked to the polymeric backbone are commonly used.<sup>[12]</sup> They are largely applied for noninvasive imaging, due to the high flexibility in molecular probes selection.<sup>[7]</sup> However, most of the molecular fluorophores are excitable in the UV–vis optical region, limiting the

penetration depth into biological tissues.<sup>[13]</sup> Furthermore, UV exposure can damage the DNA of embedded and surrounding cells.<sup>[7,14]</sup> Other limitation in the use of UV radiation is represented by a low imaging resolution due to the autofluorescence of the biological tissues overlapping to the one of fluorescent dyes.<sup>[7,15]</sup> Dyes that can be excited in the near infrared (NIR) region are alternatively considered, due to their minimal autofluorescence, which improves their detection sensitivity.<sup>[6,15,16]</sup> However, they are often chemically unstable.<sup>[7,17]</sup> In this context, upconverting nanoparticles (UCNPs) are an interesting alternative due to their ability to convert NIR radiation in UV–visible emission, through the sequential absorption of two or more photons, known as upconversion (UC) process.<sup>[5]</sup> Typical UCNPs

A. Augurio, R. Tognato, Dr. M. Alini, Prof. D. Eglin, Dr. T. Serra  
AO Research Institute Davos  
Clavadelerstrasse 8, 7270 Davos, Switzerland  
E-mail: tiziano.serra@aofoundation.org

A. Augurio, Dr. P. Cortelletti, Prof. A. Speghini  
Nanomaterials Research Group  
Department of Biotechnology  
University of Verona and INSTM  
RU Verona  
Strada Le Grazie 15, I-37314 Verona, Italy  
E-mail: adolfo.speghini@univr.it

 The ORCID identification number(s) for the author(s) of this article can be found under <https://doi.org/10.1002/aisy.201900105>.

© 2019 The Authors. Published by WILEY-VCH Verlag GmbH & Co. KGaA, Weinheim. This is an open access article under the terms of the Creative Commons Attribution License, which permits use, distribution and reproduction in any medium, provided the original work is properly cited.

DOI: 10.1002/aisy.201900105

Dr. A. Rios  
Princess Maxima Center for Pediatric Oncology  
Heidelberglaan 25, 3584 CS Utrecht, The Netherlands

Dr. R. Levato, Prof. J. Malda  
Regenerative Medicine Center and Department of Orthopaedics  
University Medical Center Utrecht  
Heidelberglaan 100, 3584CX Utrecht, The Netherlands

Dr. R. Levato, Prof. J. Malda  
Department of Equine Sciences  
Faculty of Veterinary Medicine  
Utrecht University  
Utrecht, The Netherlands

Dr. G. Giancane  
Department of Cultural Heritage  
University of Salento  
Via D. Birago, 73100 Lecce, Italy

with strong emissions in the UV–vis region upon NIR excitation are composed by lanthanide (e.g.,  $\text{Yb}^{3+}$ ,  $\text{Er}^{3+}$ ,  $\text{Tm}^{3+}$ , and  $\text{Nd}^{3+}$ ) doped inorganic fluorides (e.g.,  $\text{NaYF}_4$ ,<sup>[18]</sup>  $\text{CaF}_2$ ,<sup>[19]</sup> or  $\text{SrF}_2$ <sup>[20]</sup>) that combine efficient optical transitions with low phonon energies of the crystal host, generating strong luminescence. In terms of host matrix, fluoride-based inorganic materials are contemplated as among the best choices because of their low phonon energies and high chemical stabilities, which are advantageous properties for their potential applications as luminescent hosts.<sup>[21,22]</sup> In particular, recent research works reported that lanthanide-doped cubic  $\text{SrF}_2$  nanoparticles present higher UC emission intensities than the cubic-phase  $\text{NaYF}_4$ ,<sup>[22,23]</sup> which is among the most efficient host materials.<sup>[24]</sup> Moreover, the cubic  $\text{SrF}_2$  host shows lower phonon-energy cut-off ( $285\text{ cm}^{-1}$ ) than  $\text{NaYF}_4$  ( $360\text{ cm}^{-1}$ ). Furthermore, the ionic radius of the  $\text{Sr}^{2+}$  ions is comparable with those of the rare earth (RE) ions, facilitating the substitutional doping and the formation of cubic  $\text{SrF}_2$  structure, without notable lattice distortion.<sup>[20,22]</sup>

Moreover, compared with the traditional molecular fluorophores, UCNPs are not affected by photobleaching, have low cytotoxicity, narrow emission bands, a large anti-Stokes shift, and chemical stability,<sup>[25]</sup> and consequently are promising for in vivo tracking of hydrogels.<sup>[7,15,26]</sup>

The fabrication of UCNPs-doped hydrogel materials has been reported,<sup>[7,15,27]</sup> allowing imaging of hydrogel, although without generation of 3D-printed architectures or ability to further manipulate the hydrogel matrix. Fabrication of stimuli-responsive hydrogels has also been investigated using iron oxide nanoparticles (IONPs), which have been self-assembled and aligned into IONPs rods within hydrogels using a low magnetic field to recapitulate anisotropy of soft extracellular matrices.<sup>[4,28]</sup> Kim et al.<sup>[29]</sup> reported the fabrication of magnetic responsive microcomponent through an optofluidic maskless lithography system and a permanent magnet, where the self-assembled IONPs filaments were confined within a polyethylene glycol (PEG)/polyethylene glycol diacrylate (PEGDA) matrix of different shapes. The introduction of IONPs filaments into 3D matrices leads to a magnetic anisotropy, making the particle-laden regions controllable by external magnetic fields.<sup>[29]</sup> Thus, toward multifunctional stimuli-responsive materials, the combination of nanoparticles responsive to external stimuli within a biocompatible hydrogel matrix seems to be a promising approach. Bozuyuk et al. reported the combination of light-triggered drug delivery with magnetically controlled 3D-printed microswimmers.<sup>[30]</sup> In that work, two-photon direct laser writing was used to fabricate a magnetically powered chitosan-based helical microswimmer system that has a light-triggered drug-release capability. Even though this resulted in increased functionality and anisotropy of the microswimmers, this methodology falls short in producing objects relevant for the generation of large-scale tissue-engineered constructs.

Therefore, in this study, we present a 3D-printable optically and magnetically responsive nanocomposite hydrogel system based on a novel core@shell UCNPs-embedded gelatin methacryloyl (GelMA) laden with magnetically responsive IONPs. The UCNPs' photostability and imaging capability leads to the development of a new fluorescent nanocomposite hydrogel. By embedding IONPs-assembled filaments within the hydrogel,

it is possible to induce structural and magnetic anisotropy to the final architecture.

Previous research works demonstrated the biocompatibility of UCNPs and IONPs, which are included in biocompatible polymeric hydrogel matrix in the current research work. In particular, MTT assay, reported by Villa et al., showed no relevant cytotoxicity of Nd:  $\text{SrF}_2$  UCNPs, incubated at different concentrations (25, 50, and  $100\text{ }\mu\text{g mL}^{-1}$ ) with HeLa cells over 48 h.<sup>[20]</sup> Moreover, Bonfrate et al. evaluated by MTT assay, the potential cytotoxicity of PEG-capped IONPs, incubated with mouse fibroblast cells (NIH 3T3) for 48 h, demonstrating a cell viability close to 99%.<sup>[31]</sup> Therefore, the embedding of the aforementioned nanomaterials in highly biocompatible hydrogels should not affect their biocompatibility.

Thus, we fabricated an innovative multifunctional and multiscale nanocomposite hydrogel, which is optically and magnetically responsive, thanks to the combination of UCNPs and IONPs (Figure 1).

To create the optically responsive nanocomposite hydrogel, we designed strontium fluoride core@shell UCNPs capable of dual-NIR excitation wavelength and enhanced photostability compared with organic fluorophores. The  $\text{Yb}^{3+}$ ,  $\text{Tm}^{3+}$  ions codoped strontium fluoride core UCNPs, denoted hereafter as  $\text{SrF}_2:\text{Yb}^{3+}$ ,  $\text{Tm}^{3+}$  were prepared by a hydrothermal method<sup>[32]</sup> (Figure 2ai). The  $\text{SrF}_2:\text{Yb}^{3+}$ ,  $\text{Tm}^{3+}$  was used as a seed using the same hydrothermal method for the subsequent growth of a  $\text{Yb}^{3+}$ ,  $\text{Nd}^{3+}$ -doped strontium fluoride shell, for the preparation of core@shell UCNPs, denoted hereafter as  $\text{SrF}_2:\text{Yb}^{3+}$ ,  $\text{Tm}^{3+}@\text{SrF}_2:\text{Yb}^{3+}$ ,  $\text{Nd}^{3+}$  (Figure 2aii). The  $\text{SrF}_2:\text{Yb}^{3+}$ ,  $\text{Tm}^{3+}@\text{SrF}_2:\text{Yb}^{3+}$ ,  $\text{Nd}^{3+}$  can be activated by 980 and 800 nm excitation radiations thanks to the presence of  $\text{Yb}^{3+}$  and  $\text{Nd}^{3+}$  ions (sensitizers), respectively. The possibility to excite at 800 nm can enable safer intra-tissue and in vivo applications, as the irradiation at this wavelength has less chances to induce excitation and overheating of water, with respect to the 980 nm excitation radiation.<sup>[21,23,33]</sup> This effect is even more important especially when high irradiation power densities or long exposure times are required. Hence, 800 nm NIR allows a better penetrability in biological tissues compared with 980 nm where the high absorbance of laser radiation limits the penetration depth.<sup>[34]</sup>

The particle size distributions of  $\text{SrF}_2:\text{Yb}^{3+}$ ,  $\text{Tm}^{3+}$  core and  $\text{SrF}_2:\text{Yb}^{3+}$ ,  $\text{Tm}^{3+}@\text{SrF}_2:\text{Yb}^{3+}$ ,  $\text{Nd}^{3+}$ , dispersed in deionized  $\text{H}_2\text{O}$  ( $25\text{ mg mL}^{-1}$ ), were measured by dynamic light scattering (DLS) analysis, using a Zetasizer Nano-ZS90 instrument

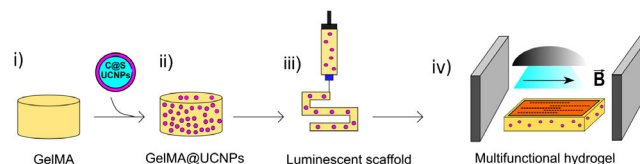


**Figure 1.** Schematic representation of 3D-printed multifunctional and multiscale controllable nanocomposite hydrogel. i,ii) Core@shell UCNPs (C@S UCNPs) were mixed with a pre-polymer solution of GelMA to obtain a luminescent ink (GelMA@UCNPs). iii) GelMA@UCNPs mixture is 3D-printed to obtain an optically responsive scaffold. iv) A solution of PEGDA IONPs is molded and the IONPs are self-assembled into a 3D-printed external chamber of GelMA@UCNPs. The UV-curing stabilize the structure of the multifunctional and multiscale organized hydrogel.

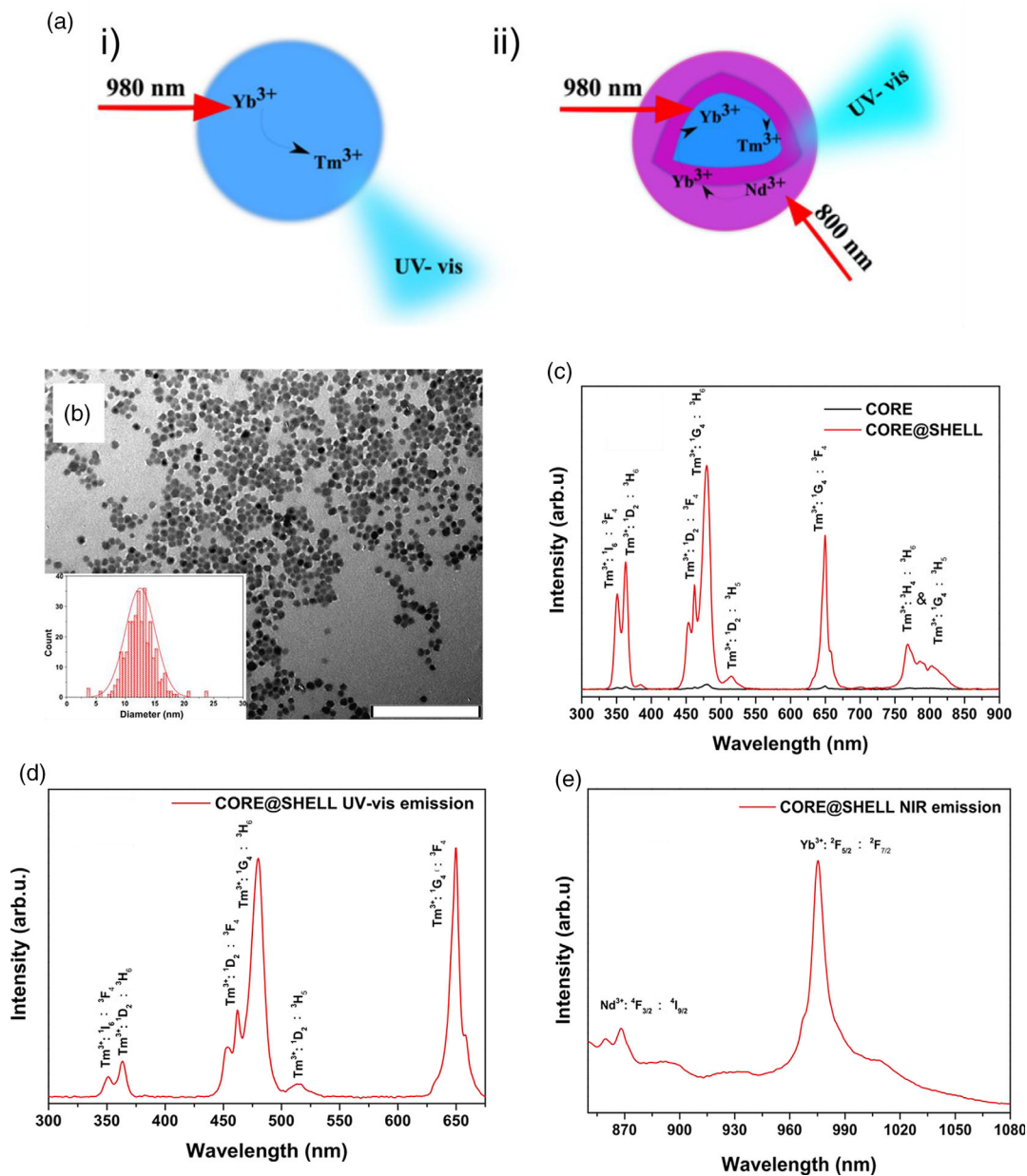


**Figure 2.** a) Schematizations of (i) UCNP core and (ii) UCNP core@shell, which can be excited, upon single (980 nm) and dual-NIR excitation radiations (800 and 980 nm), respectively. b) TEM micrograph of SrF<sub>2</sub>:Yb<sup>3+</sup>, Tm<sup>3+</sup>@SrF<sub>2</sub>:Yb<sup>3+</sup>, Nd<sup>3+</sup>, which show an average diameter size of 12.5 ± 2.5 nm (inset). Scale bar = 200 nm. c) UC emission spectrum of SrF<sub>2</sub>:Yb<sup>3+</sup>, Tm<sup>3+</sup> and SrF<sub>2</sub>:Yb<sup>3+</sup>, Tm<sup>3+</sup>@SrF<sub>2</sub>:Yb<sup>3+</sup>, Nd<sup>3+</sup> under excitation at 980 nm. d) Anti-Stokes and e) Stokes emission spectra of SrF<sub>2</sub>:Yb<sup>3+</sup>, Tm<sup>3+</sup>@SrF<sub>2</sub>:Yb<sup>3+</sup>, Nd<sup>3+</sup> upon 800 nm excitation.

(Malvern Instruments Ltd, Malvern, UK), equipped with He–Ne laser at 633 nm excitation. The SrF<sub>2</sub>:Yb<sup>3+</sup>, Tm<sup>3+</sup> core and SrF<sub>2</sub>:Yb<sup>3+</sup>, Tm<sup>3+</sup>@SrF<sub>2</sub>:Yb<sup>3+</sup>, Nd<sup>3+</sup> have average hydrodynamic diameters of 9.8 ± 2.6 and 17.4 ± 4.2 nm, respectively, (Figure S1, Supporting Information). The transmission electron microscopy (TEM) images (Philips CM200 LaB<sub>6</sub>, operating at an acceleration voltage of 200 kV) show uniform and monodispersed SrF<sub>2</sub>:Yb<sup>3+</sup>, Tm<sup>3+</sup> (Figure S2a, Supporting Information) and SrF<sub>2</sub>:Yb<sup>3+</sup>, Tm<sup>3+</sup>@SrF<sub>2</sub>:Yb<sup>3+</sup>, Nd<sup>3+</sup> (Figure 2b), with an average particle size distribution, centered at 8.2 ± 1.4 nm

(Figure S2b, Supporting Information) and 12.5 ± 2.5 nm (Figure 2b inset), respectively, according to the DLS analysis.

X-ray powder diffraction (XRD) analysis was conducted on Thermo ARL X'TRA (Thermo Fisher) X-ray diffractometer, equipped with Cu K $\alpha$  source (K $\alpha$ ,  $\lambda$  = 1.5418 Å) over 2 $\theta$  range 20°–90°. Figure S3, Supporting Information, show the XRD pattern of core SrF<sub>2</sub>:Yb<sup>3+</sup>, Tm<sup>3+</sup> and core@shell SrF<sub>2</sub>:Yb<sup>3+</sup>, Tm<sup>3+</sup>@SrF<sub>2</sub>:Yb<sup>3+</sup>, Nd<sup>3+</sup>. The diffraction peaks confirm the cubic phase of SrF<sub>2</sub> (space group Fm $\bar{3}$ m), according to the ICDD card (00-06-0262). The UC properties of SrF<sub>2</sub>:Yb<sup>3+</sup>,

$\text{Tm}^{3+}$  and  $\text{SrF}_2\text{:Yb}^{3+}$ ,  $\text{Tm}^{3+}@\text{SrF}_2\text{:Yb}^{3+}$ ,  $\text{Nd}^{3+}$  were investigated using a diode laser at 980 nm ( $@510 \text{ W cm}^{-2}$ ) and 800 nm ( $@408 \text{ W cm}^{-2}$ ) as excitation sources. The UC emission was measured in aqueous dispersions of the UCNPs (concentration of  $25 \text{ mg mL}^{-1}$ ).

The  $\text{SrF}_2\text{:Yb}^{3+}$ ,  $\text{Tm}^{3+}$  and  $\text{SrF}_2\text{:Yb}^{3+}$ ,  $\text{Tm}^{3+}@\text{SrF}_2\text{:Yb}^{3+}$ ,  $\text{Nd}^{3+}$ , generate an UV-vis emission, under NIR excitation radiations (800 and 980 nm), due to the presence of  $\text{Nd}^{3+}$  and  $\text{Yb}^{3+}$  dopant ions as sensitizer and  $\text{Tm}^{3+}$  ion as activator.

Upon 980 nm excitation, the UC emission is due to energy-transfer processes between  $\text{Yb}^{3+}$ ,  $\text{Nd}^{3+}$ , and  $\text{Tm}^{3+}$ . In particular, the UV emission bands centered at 348 and 365 nm, are attributed to the  $^1\text{I}_6 \rightarrow ^3\text{F}_4$  and  $^1\text{D}_2 \rightarrow ^3\text{H}_6$  electronic transitions of  $\text{Tm}^{3+}$  ion, respectively, whereas the blue visible emission ones located at 453, 480, 650, 770, and 800 nm are due to the  $^1\text{D}_2 \rightarrow ^3\text{F}_4$ ,  $^1\text{G}_4 \rightarrow ^3\text{H}_6$ ,  $^1\text{G}_4 \rightarrow ^3\text{F}_4$ ,  $^1\text{G}_4 \rightarrow ^3\text{H}_5$ ,  $^3\text{H}_4 \rightarrow ^3\text{H}_6$  transitions of  $\text{Tm}^{3+}$  ion, respectively. The luminescence intensity of the  $\text{SrF}_2\text{:Yb}^{3+}$ ,  $\text{Tm}^{3+}@\text{SrF}_2\text{:Yb}^{3+}$ ,  $\text{Nd}^{3+}$  are much higher than for the  $\text{SrF}_2\text{:Yb}^{3+}$ ,  $\text{Tm}^{3+}$  (Figure 2c), due to the presence of an active shell on the core UCNPs, allowing a much better harvesting of 980 nm radiation. Moreover, the shell part reduces the nonradiative multiphonon relaxation processes for the lanthanide ions that are due to interaction with high-energy phonons of water molecules, and therefore the luminescence intensity due to  $\text{Tm}^{3+}$  ions becomes much more intense.<sup>[35]</sup> Under 800 nm excitation, the  $\text{SrF}_2\text{:Yb}^{3+}$ ,  $\text{Tm}^{3+}@\text{SrF}_2\text{:Yb}^{3+}$ ,  $\text{Nd}^{3+}$  show an UC emission, generated by an energy-transfer mechanism between  $\text{Tm}^{3+}$  (activator),  $\text{Yb}^{3+}$  (bridge), and  $\text{Nd}^{3+}$  (sensitizer). UC emission bands in the UV region, centered at 348 and 365 nm, are due to  $^1\text{I}_6 \rightarrow ^3\text{F}_4$  and  $^1\text{D}_2 \rightarrow ^3\text{H}_6$   $\text{Tm}^{3+}$  ions transitions, whereas visible emissions at 453, 480, 650 nm, are assigned to  $^1\text{D}_2 \rightarrow ^3\text{F}_4$ ,  $^1\text{G}_4 \rightarrow ^3\text{H}_6$ ,  $^1\text{G}_4 \rightarrow ^3\text{F}_4$  transitions (Figure 2d).

In addition,  $\text{SrF}_2\text{:Yb}^{3+}$ ,  $\text{Tm}^{3+}@\text{SrF}_2\text{:Yb}^{3+}$ ,  $\text{Nd}^{3+}$  exhibit Stokes emission bands at 870 and 980 nm (Figure 2e), due to the  $^4\text{F}_{3/2} \rightarrow ^4\text{I}_{9/2}$  and  $^2\text{F}_{5/2} \rightarrow ^2\text{F}_{7/2}$ , transitions of  $\text{Nd}^{3+}$  and  $\text{Yb}^{3+}$  ions, respectively.

To create the optically responsive hydrogel, the  $\text{SrF}_2\text{:Yb}^{3+}$ ,  $\text{Tm}^{3+}@\text{SrF}_2\text{:Yb}^{3+}$ ,  $\text{Nd}^{3+}$  have been selected as luminescent probes, thanks to their ability to be excited upon 800 nm. Thus,  $\text{SrF}_2\text{:Yb}^{3+}$ ,  $\text{Tm}^{3+}@\text{SrF}_2\text{:Yb}^{3+}$ ,  $\text{Nd}^{3+}$  were combined with GelMA hydrogel, synthesized as reported in previous study<sup>[36]</sup> (Supporting Information), creating a nanocomposite hydrogel, named hereafter G@UCNPs. GelMA ( $200 \text{ mg mL}^{-1}$ ) and the photoinitiator Irgacure 2959 ( $3 \text{ mg mL}^{-1}$ ) were mixed directly into a homogeneous suspension of UCNPs ( $25 \text{ mg mL}^{-1}$ ) in PBS. The cytocompatibility of photoinitiators is an important parameter to consider in the photo-crosslinking process for cells encapsulation. Mironi-Harpaz et al. reported relatively high survival rates of bovine aortic smooth muscle cells (SMCs)-encapsulating hydrogels after photo-polymerization, in the presence of Irgacure 2959 as photoinitiator at a concentration of 0.2% (w/w).<sup>[37]</sup> In addition, another research work showed a reasonable cytocompatibility of Irgacure 2959 at different concentrations (0, 0.03, 0.05, 0.1% w/v) over a wide range of cell types, confirming its low toxicity.<sup>[38]</sup> Therefore, Irgacure 2959 was chosen as photoinitiator for photo-crosslinking of GelMA hydrogel. The solution was then heated at  $70^\circ\text{C}$  to allow the complete dissolution of GelMA and then vortexed until a homogeneous suspension was obtained. Hydrogel was cross-linked

with UV-irradiation (UV-A, 365 nm,  $0.1 \text{ J cm}^{-2}$ , Vilber Lourmat, Collégien, France) for 5 min.

The stability of UCNPs within GelMA matrix was analyzed using UC spectroscopy. The G@UCNPs sample, placed in a quartz cuvette, was incubated in PBS and the UC spectra were recorded at 1, 6, and 24 h, upon 980 nm as excitation source. The UC emission profiles, reported in Figure S5, Supporting Information, show that no evident decrease in the emission intensities obtained over 24 h, demonstrating the negligible UCNPs release from the polymeric matrix.

The possibility to excite G@UCNPs upon 800 nm excitation source allows the remote tracking of nanocomposite scaffold (Figure 3).

Recently, GelMA has been extensively used for the fabrication of complex structures via extrusion-based 3D-printing.<sup>[39]</sup> In an extrusion-based 3D printing process, the viscosity of the ink should decrease quickly as a shear is applied, whereas a fast recovery in the viscosity of the ink is required after the layer deposition to retain the printed structure.<sup>[40]</sup> The G@UCNPs nanocomposite ink was produced as described previously, and the rheological properties of the G@UCNPs luminescent ink were assessed with an Anton Paar MCM 302 rheometer, by rotational measurement (shear rate interval  $0.01\text{--}100 \text{ s}^{-1}$ , parallel geometry PP-25, gap size 0.4 mm,  $T = 25^\circ\text{C}$ ). The flow curve of the nanocomposite ink evidence a rapid decrease in viscosity with an increasing shear rate demonstrating the shear-thinning behavior of the newly developed material essential for an extrusion-based 3D-printing process (Figure 3a). Moreover, the almost perfect overlap in the flow curve of G@UCNPs ink with the control, GelMA, excludes any additional strong physical interaction between the encapsulated nanoparticles and the polymeric matrix.

Subsequently, a flower-like structure and a quadricula, with a total side length of 1 cm were designed and sliced with the 3D model slicer (BioCAM, regenHU, Ltd) (Figure 3bi,ii). The generated paths were then used to instruct an extrusion-based 3D-printer (3D Discovery instrument, regenHU Ltd). The printing process was performed in a temperature range of  $25\text{--}30^\circ\text{C}$ , using a 3–4 bar pressure and a Teflon-covered needle (0.3 mm inner diameter). Once printed, the G@UCNPs hydrogel structures were photo-polymerized as described previously allowing the final stabilization of the shapes. The printing process generates stable structures with different geometries and well-defined pores as shown in Figure 3biii,iv. The flower-like 3D-printed structures were imaged with a dual-platform confocal laser scanning/multiphoton microscope Zeiss 880 (Carl Zeiss, Germany), equipped with a Mai Tai TI:Sapphire laser source (Spectra-Physics, USA), by irradiating with an 800 nm excitation wavelength as reported in the schematic (Figure 3c). The UC properties of G@UCNPs were investigated using a diode laser at 980 nm as excitation source. The UC spectrum of G@UCNPs shows UC emission bands in the visible region, centered at 453, 480, and 650 nm, which are referred to  $^1\text{D}_2 \rightarrow ^3\text{F}_4$ ,  $^1\text{G}_4 \rightarrow ^3\text{H}_6$ ,  $^1\text{G}_4 \rightarrow ^3\text{F}_4$  transitions (Figure 3d).

This blue-light emission of UCNPs was then used to image the 3D-printed shapes. (Figure 3e, Video S1, Video S2, Video S3, Supporting Information). To simulate a deep-tissue imaging condition, the 3D-printed shapes were then placed beneath  $\approx 0.6 \text{ mm}$  layer of chicken breast muscle, and then imaged upon excitation at

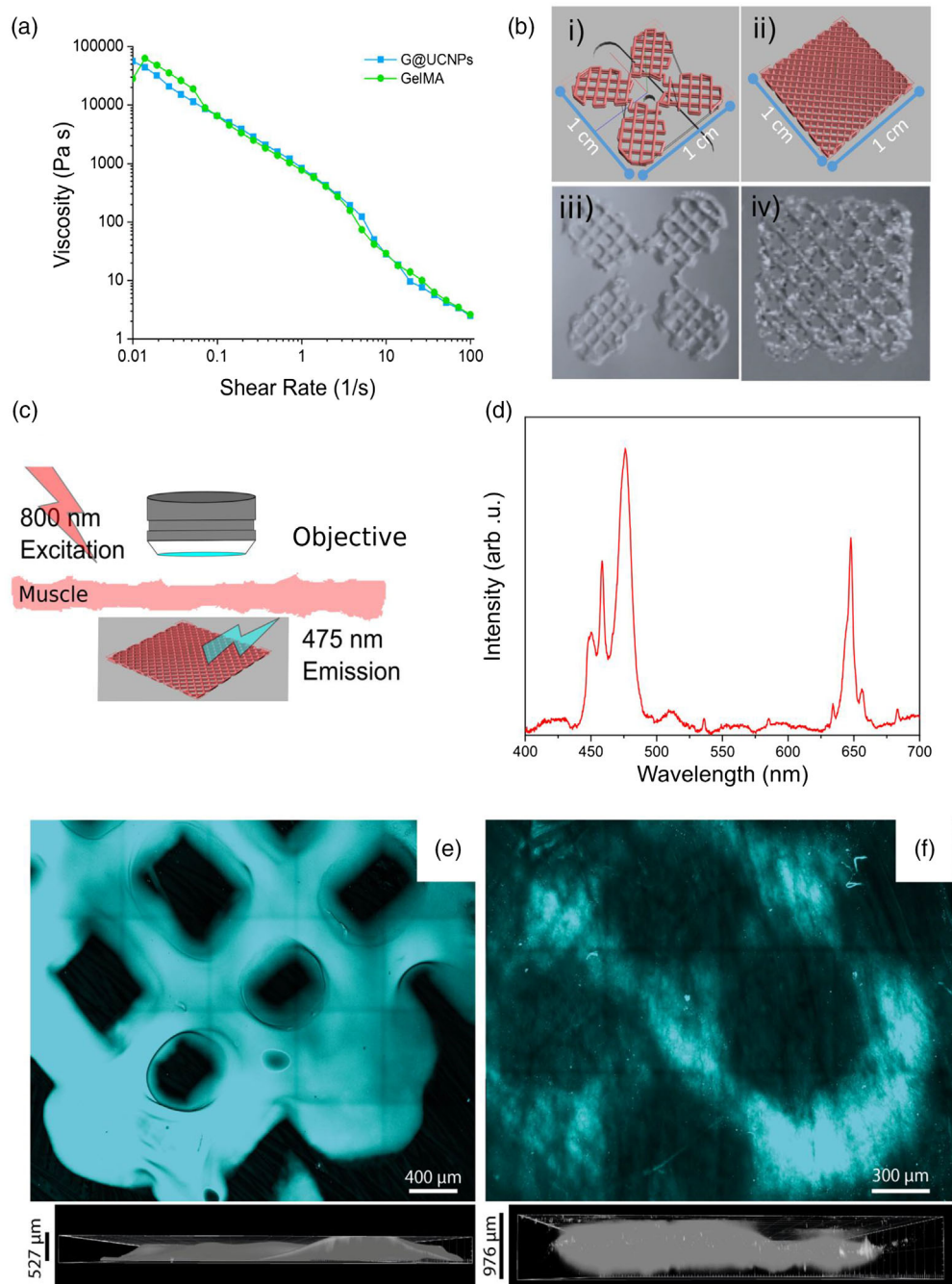


**Figure 3.** a) Flow-curve of GelMA and G@UPCNPs mixture. b–i,ii) Slicing of the structures. iii,iv) Flower-like shape and quadricula 3D-printed structures. c) Schematic of 3D-printed GelMA@UCNPs scaffold hydrogel imaged beneath a simulated muscles tissue. d) UC emission spectrum of UCNPs core@-shell, upon excitation at 980 nm. e) Maximum projection of directly imaged pristine hydrogel-particle composite structures and f) of composite hydrogels imaged below chicken breast muscle.

800 nm. The  $\text{SrF}_2:\text{Yb}^{3+}, \text{Tm}^{3+}$  @  $\text{SrF}_2:\text{Yb}^{3+}, \text{Nd}^{3+}$  were shown suitable for deep-tissue in situ scaffold monitoring via infrared stimulation, as the emission signal was high enough to visualize the 3D-printed hydrogel structure also when an optically opaque dead muscle tissue was placed between the microscope objective and the sample. In particular, the printed mesh was easily visible despite the signal attenuation caused by the muscle layer and its

autofluorescence. (Figure 3f, Video S4, Supporting Information). Imaging below thicker tissue slices should also be possible, given the excitation/emission profile of the UCNPs, although it would require a different imaging system, as the microscope used herein has the focal distance of the objective a limiting factor.

To introduce additional functionalities, magnetic-responsive IONPs are combined to the optically responsive G@UCNPs

hydrogel to produce a multifunctional hydrogel, using the magnetic self-assembly of IONPs in hydrogel to introduce anisotropy at the meso- and nanoscale.<sup>[4,30,41]</sup> The G@UCNPs were printed with an empty inner portion, which acts as assembly chamber for the magnetic nanoparticles (Figure 1). The outer cases composed of G@UCNPs, which is solid at  $T < 37\text{ }^{\circ}\text{C}$ , was filled up with a solution of PEGDA monomer (liquid), the photoinitiator Irgacure 2959 ( $3\text{ mg mL}^{-1}$ ), and IONPs ( $\approx 2.5\text{ mg mL}^{-1}$ ). To trigger the assembly of the IONPs into filaments, the assembly chambers and G@UCNPs filled with PEGDA/IONPs solution, were then placed between two commercially available neodymium permanent magnets spaced at 5 cm from each other. The assembly was hence directed by the zero gradient and static magnetic fields with an intensity of  $0.02\text{ T}$ .<sup>[27]</sup> Once the IONPs assembling was completed, the entire macrostructure was stabilized by photo-crosslinking of the acrylic groups via UV-light exposure, obtaining a hierarchically structured hybrid nanocomposite endowed with differential functionality. The entire structure of our newly developed multifunctional hydrogel is stabilized with the photo-induced cross-linking of the acrylate groups present on PEGDA and GelMA (Figure 4a,b). Recently, similar techniques of photo-induced cross-linking have

been successfully used for the fabrication of multi-layered hydrogels with complex architecture. Nguyen et al. reported the production of physically, chemically, and spatially organized biomaterial, obtained by a layer-by-layer deposition to resemble the complex multi-layered cartilage structure. The photo-crosslinking process was used to partially cross-link, and subsequently to connect covalently every consecutive layer through acrylate group present in the macromer solution to obtain a hierarchically structured 3D hydrogel, which retains its mechanical stability over six weeks.<sup>[42]</sup> Moreover, the modularity of the multifunctional hydrogel fabrication process allows assembling the IONPs along several directions within the external cases, providing the overall structure with different preferential axis of magnetization (Figure 4c).<sup>[28,43]</sup> The presented manufacturing process is extendable to a wide set of hydrogel and monomer solutions as long as the outer layer can act as an assembly chamber for the second component, and the two subunits can be physically or chemically cross-linked together.

In the first instance, the IONPs release from the polymeric matrix was monitored by means of atomic absorption spectroscopy. Three samples of the nanocomposite hydrogel were incubated in PBS at  $37\text{ }^{\circ}\text{C}$  for 24 h. An aliquot of PBS was recovered

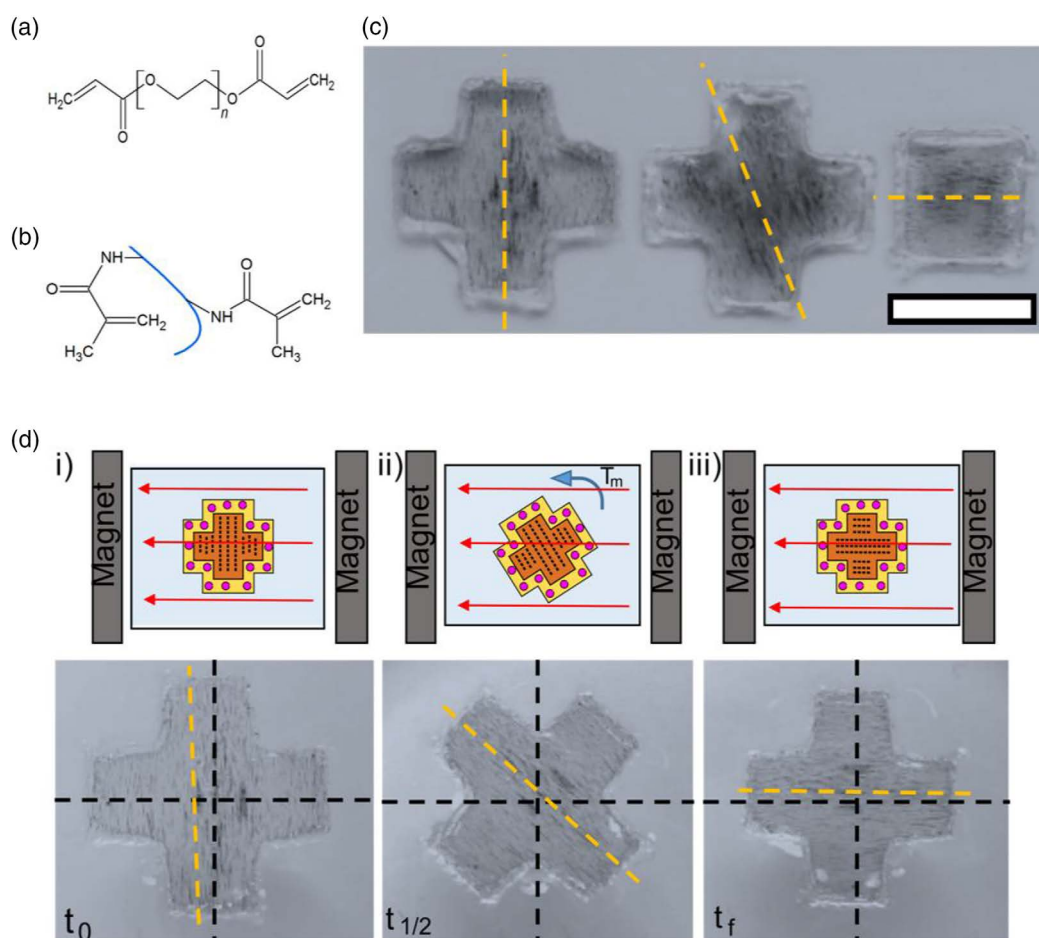


**Figure 4.** a) Molecular structure of the PEGDA and b) gelatin methacrylate. c) Fabricated structures with different IONPs alignment axis with respect to the outer case (Scale bar = 1 cm). d) Image sequence of a fabricated structure controlled by an external magnetic field at i)  $t_0$ , ii)  $t_{1/2}$ , and iii)  $t_f$ . (Video S5, Supporting Information).

and analyzed after 6, 9, and 24 h of incubation, and the amount of iron content was evaluated through atomic absorption spectroscopy by means of Varian spectrAA-600. The iron-release kinetic was reported in Figure S6, Supporting Information. Iron detected after 24 h was about 44.5 ppb that is less than  $0.05 \mu\text{g mL}^{-1}$ , a concentration that can be considered not toxic for the metabolic activity of the cell.<sup>[44]</sup>

In addition, to verify the magnetic response of the hybrid material, the entire structure was subjected to an external static magnetic field, while floating on the water surface. Initially, it was positioned with the easy magnetization axis perpendicular to the field line. The resulting magnetic torque,  $T_m$ , induces the structure rotation along the vertical axis of the geometry structures (intersection between the black dashed line), until an alignment of the magnetization axis with the fields line was reached (Figure 4d–i, ii, iii).<sup>[28,43,45]</sup> Thanks to the external magnetic stimuli, this resulted hydrogel can be remotely controlled and used for a broad range of biomedical applications, such as noninvasive triggering of drug-release processes. The fabrication of magnetic- and light-responsive hydrogel is a promising example of novel nanocomposite material, that could be used for a wide range of applications. The incorporation of nanoparticles in the gel network allows the formation of an hybrid material with synergic properties, which arise from both the components.<sup>[46,47]</sup> Research works have reported the application of light-responsive gels for hydrogel degradation, accompanied by molecular release, which has great importance for drug delivery.<sup>[48]</sup> In addition, the introduction of photoresponsive superhydrophobic component on a hydrogel surface has been reported as innovative mechanism to regulate substances' diffusion between hydrogel and external microenvironment.<sup>[49]</sup> Other research works have presented the use of magnetically responsive droplets for switchable remote and noninvasive controllability, which is a potential requirement for many biomedical applications.<sup>[50]</sup> Therefore, considering the light and magnetic responsiveness, the developed bifunctional hydrogel enhances the applicability of this innovative material in biomedical application. In conclusion, the combination of additive manufacturing technology, bioimaging, and magnetic self-assembly process permits the development of an optically and magnetically responsive nanocomposite hydrogel with anisotropic features within hierarchically organized architectures. The optical functionality is given by core@shell UCNPs, which emit UV–vis light upon double wavelength excitation (800 and 980 nm). The luminescent nanocomposite hydrogel is printable and can be used to create hierarchically complex 3D structures. Moreover, the incorporation of magnetically aligned IONPs, allow the multiscale organization of the novel material. The synergistic effect of optical and magnetic properties into 3D-printed structures, represents a compelling example of multiscale organized material, which opens the way to future studies in real-time deep monitoring and remote manipulation.

## Supporting Information

Supporting Information is available from the Wiley Online Library or from the author.

## Acknowledgements

The authors would like to thank University of Verona ("Ricerca di base 2015" project) and Dutch Arthritis Society (ReumaNederland; LLP-12, LLP-22) for their financial support.

## Conflict of Interest

The authors declare no conflict of interest.

## Keywords

deep tracking, multifunctional, multiscale, remote control, upconversion

Received: September 5, 2019

Revised: November 15, 2019

Published online: December 29, 2019

- [1] J. R. Greer, J. Park, *Nano Lett.* **2018**, *18*, 2187.
- [2] K. Saloniitis, J. Pandremenos, J. Paralikas, G. Chryssoulouris, *Int. J. Adv. Manuf. Technol.* **2010**, *49*, 803.
- [3] P. Thoniyot, M. J. Tan, A. A. Karim, D. J. Young, *Adv. Sci.* **2015**, *2*, 1.
- [4] R. Tognato, A. R. Armiento, V. Bonfrate, R. Levato, J. Malda, M. Alini, D. Eglin, G. Giancane, T. Serra, *Adv. Funct. Mater.* **2018**, *1804647*, 1.
- [5] B. Yan, J. Boyer, D. Habault, N. R. Branda, Y. Zhao, *J. Am. Chem. Soc.* **2012**, 16558.
- [6] M. L. Viger, M. Grossman, N. Fomina, A. Almutairi, *Adv. Mater.* **2013**, *25*, 3733.
- [7] Y. Dong, G. Jin, C. Ji, R. He, M. Lin, X. Zhao, A. Li, T. J. Lu, F. Xu, *Acta Biomater.* **2017**, *55*, 410.
- [8] G. Jalani, R. Naccache, D. H. Rosenzweig, S. Lerouge, L. Haglund, F. Vetrone, M. Cerruti, *Nanoscale* **2015**, *7*, 11255.
- [9] R. Liu, X. Zou, Y. Xu, X. Liu, Z. Li, *Chem. Lett.* **2016**, 1054.
- [10] J. Shao, Y. Huang, Q. Fan, *Polym. Chem.* **2014**, 4195.
- [11] R. Liu, H. Chen, Z. Li, F. Shi, X. Liu, *Polym. Chem.* **2016**, 2457.
- [12] F. J. Pedraza, J. C. Avalos, B. G. Yust, Y. Dong, M. Lin, G. Jin, Y. Il Park, M. Qiu, *Nanotechnology* **2017**, *28*, 175702.
- [13] K. Szaciłowski, W. Macyk, A. Drzewiecka-Matuszek, M. Brindell, G. Stochel, *Chem. Rev.* **2005**, *105*, 2647.
- [14] S. Wu, H. J. Butt, *Adv. Mater.* **2016**, *28*, 1208.
- [15] G. Jalani, R. Naccache, D. H. Rosenzweig, S. Lerouge, L. Haglund, F. Vetrone, M. Cerruti, *Nanoscale* **2015**, 11255.
- [16] A. M. Smith, M. C. Mancini, S. Nie, *Nat. Nanotechnol.* **2009**, *4*, 710.
- [17] D. Wang, J. Qian, S. He, J. S. Park, K. S. Lee, S. Han, Y. Mu, *Biomaterials* **2011**, *32*, 5880.
- [18] B. R. Kumar, M. Nyk, T. Y. Ohulchanskyy, C. A. Flask, P. N. Prasad, *Adv. Funct. Mater.* **2009**, *19*, 853.
- [19] N. Dong, M. Pedroni, F. Piccinelli, G. Conti, A. Sbarbati, L. Marti, M. Carmen, I. Cruz, J. E. Rami, F. Sanz-rodriguez, A. Juarraz, F. Chen, F. Vetrone, J. A. Capobianco, *ACS Nano* **2011**, *5*, 8665.
- [20] I. Villa, A. Vedda, I. X. Cantarelli, M. Pedroni, F. Piccinelli, M. Bettinelli, A. Speghini, M. Quintanilla, F. Vetrone, U. Rocha, C. Jacinto, E. Carrasco, J. G. Solé, D. J. García, *Nano Res.* **2015**, *8*, 649.
- [21] D. Przybylska, *Sci. Rep.* **2019**, 1.
- [22] J. S. Sinju, T. L. Anbharasi, D. Sarkar, V. N. K. B. Adusumalli, *J. Mater. Sci. Mater. Electron.* **2019**.
- [23] M. Quintanilla, I. X. Cantarelli, M. Pedroni, A. Speghini, F. Vetrone, *J. Mater. Chem. C* **2015**, *3*, 3108.
- [24] C. Shell, S. Nanoparticles, H. Wen, H. Zhu, X. Chen, T. F. Hung, B. Wang, G. Zhu, S. F. Yu, F. Wang, *Angew. Chemie Int. Ed.* **2013**, *52*, 13419.

- [25] S. Beyazit, S. Ambrosini, N. Marchyk, E. Palo, V. Kale, T. Soukka, B. Tse Sum Bui, K. Haupt, *Angew. Chem. Int. Ed.* **2014**, *53*, 8919.
- [26] L. Yongsheng, T. Datao, Z. Haomiao, C. Xueyuan, *Chem. Soc. Rev.* **2013**, *42*, 6924.
- [27] C. Ye, J. Ma, S. Chen, J. Ge, W. Yang, Q. Zheng, X. Wang, Z. Liang, Y. Zhou, *J. Phys. Chem. C* **2017**, *121*, 20158.
- [28] K. Hu, J. Sun, Z. Guo, P. Wang, Q. Chen, M. Ma, N. Gu, *Adv. Mater.* **2015**, *27*, 2507.
- [29] J. Kim, S. E. Chung, S. Choi, H. Lee, J. Kim, S. Kwon, *Nat. Mater.* **2011**, *10*, 747.
- [30] U. Bozuyuk, O. Yasa, I. C. Yasa, H. Ceylan, S. Kizilel, M. Sitti, *ACS Nano* **2018**, *12*, 9617.
- [31] V. Bonfrate, D. Manno, A. Serra, L. Salvatore, A. Sannino, A. Buccolieri, T. Serra, G. Giancane, *J. Colloid Interface Sci.* **2017**, *501*, 185.
- [32] M. Pedroni, F. Piccinelli, T. Passuello, S. Polizzi, J. Ueda, P. Haro-González, L. M. Maestro, D. Jaque, J. García-Solé, M. Bettinelli, A. Speghini, *Cryst. Growth Des.* **2013**, *2*, 4906.
- [33] M. V. DaCosta, S. Doughan, Y. Han, U. J. Krull, *Anal. Chim. Acta* **2014**, *832*, 1.
- [34] B. Rosal, A. Pérez-delgado, M. Misiak, A. Bednarkiewicz, A. S. Vanetsev, D. J. Jovanović, M. D. Dramićanin, U. Rocha, K. U. Kumar, C. Jacinto, E. Navarro, E. M. Rodríguez, M. Pedroni, A. Speghini, G. A. Hirata, I. R. Martín, D. Jaque, M. Misiak, A. Bednarkiewicz, B. Rosal, P. Alberto, A. S. Vanetsev, Y. Orlovskii, D. J. Jovanovic, M. D. Dramic, *J. Appl. Phys.* **2015**, *118*, 143104.
- [35] R. Arppe, I. Hyppänen, N. Perälä, R. Peltomaa, M. Kaiser, C. Würth, S. Christ, U. Resch-Genger, M. Schäferling, T. Soukka, *Nanoscale* **2015**, *7*, 11746.
- [36] J. W. Nichol, S. T. Koshy, H. Bae, C. M. Hwang, S. Yamanlar, A. Khademhosseini, *Biomaterials* **2010**, *31*, 5536.
- [37] I. Mironi-harpaz, D. Yingquan, S. Venkatraman, D. Seliktar, *Acta Biomater.* **2012**, *8*, 1838.
- [38] C. G. Williams, A. N. Malik, T. Kyun, P. N. Manson, J. H. Elisseeff, *Biomaterials* **2005**, *26*, 1211.
- [39] I. T. Ozbolat, M. Hospodiuk, *Biomaterials* **2015**, *76*, 321.
- [40] S. Ji, M. Guvendiren, *Front. Bioeng. Biotechnol.* **2017**, *5*, 1.
- [41] M. M. Schmauch, S. R. Mishra, B. A. Evans, O. D. Velev, J. B. Tracy, *ACS Appl. Mater. Interfaces* **2017**, *9*, 11895.
- [42] L. H. Nguyen, A. K. Kudva, N. S. Saxena, K. Roy, *Biomaterials* **2011**, *32*, 6946.
- [43] R. M. Erb, J. J. Martin, R. Soheilian, C. Pan, J. R. Barber, *Adv. Funct. Mater.* **2016**, *26*, 3859.
- [44] S. H. Doak, *Nano Rev.* **2010**, *1*, 1.
- [45] D. Morales, B. Bharti, M. D. Dickey, O. D. Velev, *Small* **2016**, *12*, 2283.
- [46] G. Huang, F. Li, X. Zhao, Y. Ma, Y. Li, M. Lin, G. Jin, T. J. Lu, G. M. Genin, F. Xu, *Chem. Rev.* **2017**, *117*, 12764.
- [47] S. Bhattacharya, S. K. Samanta, *Chem. Rev.* **2016**, *116*, 11967.
- [48] Y. Dong, G. Jin, Y. Hong, H. Zhu, T. J. Lu, F. Xu, D. Bai, M. Lin, *ACS Appl. Mater. Interfaces* **2018**, *10*, 12374.
- [49] L. Chen, X. Yao, Z. Gu, K. Zheng, C. Zhao, W. Lei, Q. Rong, L. Lin, J. Wang, L. Jiang, M. Liu, *Chem. Sci.* **2017**, *8*, 2010.
- [50] G. Huang, M. Li, Q. Yang, Y. Li, H. Liu, H. Yang, F. Xu, *ACS Appl. Mater. Interfaces* **2017**, *9*, 1155.